Available online at www.sciencedirect.com
ScienceDirect
Journal of Power Sources 165 (2007) 803–813
JOURNAL OF POWER SOURCES
www.elsevier.com/locate/jpowsour

Design for geometric parameters of PEM fuel cell by integrating computational fluid dynamics code with optimization method

Chin-Hsiang Cheng [a,*], Hung-Hsiang Lin [b], Guang-Jer Lai [b]

[a] *Department of Aeronautics and Astronautics, National Cheng Kung University, No.1, Ta Shieh Road, Tainan, Taiwan 70101, ROC*
[b] *Department of Mechanical Engineering, Tatung University, Taipei, Taiwan 10451, ROC*

Received 30 October 2006; received in revised form 20 December 2006; accepted 20 December 2006
Available online 30 December 2006

Abstract

The present study is aimed at optimization of the geometric parameters of the proton exchange membrane (PEM) fuel cells through numerical simulation. The approach is developed by integrating a direct problem solver with an optimizer. A commercial computational fluid dynamics code is used as the direct problem solver, which is used to simulate the three-dimensional mass, momentum and species transport phenomena as well as the electron- and proton-transfer process taking place in a PEMFC. On the other hand, the simplified conjugate-gradient method (SCGM) is employed to build the optimizer, which is combined with the direct problem solver in order to seek the optimal geometric parameters, including, for example, the gas channel width fraction, the gas channel height and the thickness of the gas diffusion layer. It is found that the present approach can be applied to determine the optimal set of geometric parameters, and the search process is robust and always leads to a unique final solution regardless of the initial guess.

Keywords: PEM fuel cell; Optimization; Geometric design; SCGM

1. Introduction

Numerical methods have been employed to study the physical phenomenon of interest in the fuel cells since these methods require relatively lower cost for analysis than the experimental ones. Furthermore, they in general provide a sufficient amount of data not easily obtainable with measurements. Thus, important natures of the flow and the thermal fields might then be observed and discussed extensively by numerical studies. To name a few, Wang and Savinell [1] performed a simulation of the effects of porosity and thickness of the catalyst layer, Pt loading and CO poisoning on fuel cells. Yi and Nguyen [2] used the numerical methods to solve a two-dimensional single-phase PEMFC model with interdigitated flow channels so as to evaluate the effects of inlet and exit pressures, gas diffusion layer thickness and carbon plate width on the performance of PEMFC. Gurau et al. [3] developed a half-cell model to deal with the transport phenomena at the cathode of the PEMFC. The research explored the effects of the porosity of the gas diffusion layer on the performance of fuel cells. A transient model has been developed by Um et al. [4] to simulate proton exchange membrane fuel cells by accounting simultaneously for electrochemical kinetics, current distribution, hydrodynamics and multicomponent transport. A two-dimensional cross-the-channel model was applied by Sun et al. [5] to investigate the influence of gas diffusion layer (GDL) property and flow-field geometry on the local reaction rate in the PEMFC cathode catalyst layer.

As to the three-dimensional models, Hontanon et al. [6] adopted a commercial computational fluid dynamics code (FLUENT) to predict the effects of a group of geometrical parameters on the polarization performance of the fuel cells. Berning and Djilali [7] used a three-dimensional physical model to evaluate the performance of the fuel cells at different operating conditions. Their research showed that an increase in the fuel cell temperature could raise the cell exchange current density, ionic conductivity of proton exchange membrane, gas diffusivity, and the operating voltage and then lead to an increase in the cell performance. A detailed review regarding the CFD modeling and related experimental validation has been given by Wang [8].

* Corresponding author. Tel.: +886 6 2757575x63627; fax: +886 6 2389940.
E-mail address: chcheng@mail.ncku.edu.tw (C.-H. Cheng).

0378-7753/$ – see front matter © 2007 Elsevier B.V. All rights reserved.
doi:10.1016/j.jpowsour.2006.12.040

Nomenclature

a	water activity
D	mass diffusivity ($cm^2\ s^{-1}$)
e	design parameter
F	Faraday constant, 96,487 $C\ mol^{-1}$
h	height of gas channel (m)
i	local electric current density ($A\ m^{-2}$)
$\bar{i}$	local ionic current density ($A\ m^{-2}$)
$\mathbf{I}$	electric current density ($A\ m^{-2}$)
j	transfer current density ($A\ m^{-3}$)
J	objective function
k	permeability (m^2)
l_C	gas channel width (m)
l_L	gas channel length (m)
l_P	width of a module (m)
M	molecular weight ($kg\ kmol^{-1}$)
n	coordinate in the direction normal to the surface
P	pressure (Pa)
$\mathbf{P}$	power density ($W\ m^{-2}$)
r	concentration parameter
R	universal gas constant, 8.314 $J\ mol^{-1}\ K^{-1}$
S	source term in species equation
t_{GDL}	thickness of gas diffusion layer (m)
t_{Cat}	thickness of catalyst layer (m)
t_m	thickness of membrane (m)
t_P	thickness of carbon plate (m)
T	temperature (K)
$\vec{U}$	gas velocity vector ($m\ s^{-1}$)
V	inlet gas velocity ($m\ s^{-1}$)
$\mathbf{V}$	cell voltage (V)
X	mole fraction
x, y, z	Cartesian coordinates
Y	mass fraction

Greek symbols

$\Gamma_{S,Cat}$	ionic conductivity of solid catalyst particle ($\Omega^{-1}\ m^{-1}$)
Γ_m	ionic conductivity of membrane ($\Omega^{-1}\ m^{-1}$)
Λ	gas channel width fraction
α	transfer coefficient for the reaction
β	step size
γ	conjugate-gradient coefficient
χ	Bruggemann coefficient
ε_{GDL}	porosity of gas diffusion layer
$\varepsilon_{V,Cat}$	porosity of catalyst layer
ϕ	electric potential (V)
φ	phase potential (V)
λ	membrane water content (kmol H_2O (kmol SO_3^-)$^{-1}$)
ρ	density of oxygen ($kg\ m^{-3}$)
σ_{GDL}	electronic conductivity of gas diffusion layer ($\Omega^{-1}\ m^{-1}$)
σ_P	electronic conductivity of carbon plate ($\Omega^{-1}\ m^{-1}$)
$\sigma_{S,Cat}$	electronic conductivity of solid catalyst particle ($\Omega^{-1}\ m^{-1}$)
τ	fluid stress ($N\ m^{-2}$)
ζ	source term in electronic conduction equation

Subscripts

a	anode
c	cathode/gas channel
Cat	catalyst layer
eff	effective
GDL	gas diffusion layer
i	inlet
m	membrane
N	Nafion
o	outlet
P	carbon plate
ref	reference
S	solid catalyst particles

From a survey of existing numerical studies, it is readily noted that most of the reports were focused on simulation of the transport phenomenon in a PEM fuel cell, or at most on parametric study of the effects of physical variables. Although there is a growing body of literature on the PEM fuel cells, very few reports dealt with the optimization of the design parameters. Among these studies, Mohamed and Jenkins [9] used the genetic algorithm to determine the configuration of the PEM fuel. Grujicic and Chittajallu [10] proposed a non-linear constrained optimization procedure used in the cathode design in order to maximize the average current density at a fixed voltage in a PEM fuel cell with interdigitated gas distributors. Optimization was performed for the better catalyst layer composition by Secanell et al. [11] using a two-dimensional model and a multivariable optimization technique.

Recently, Lin et al. [12] investigated the optimization of the proton exchange membrane fuel cell based on a two-dimensional cathode model. Optimization method was employed to determine the optimal combination of the design parameters, including the channel width ratio, the porosity of GDL and the porosity of the catalyst layer. However, the two-dimensional half-cell model used by the authors is rather straightforward and not able to simulate the complex three-dimensional physical transport phenomena in a PEM fuel cell.

In theory, the task of optimization is basically performed to search for a combination of the most appropriate values of a number of design parameters so that a defined objective function could be minimized. Nowadays, numerous useful optimization methods are available, for example, the genetic algorithm [9], the conjugate-gradient method (CGM) [13], the Newton-Raphson method [14], the adaptive weighting input estimation method [15] and so on. Modifications of the traditional conjugate-gradient method were proposed by Cheng and Chang [13], and the approach is named the simplified conjugate-gradient method (SCGM). In the SCGM method, there is no need to solve the

simultaneous equations for the step sizes and the complexity in mathematical manipulation and the constraint of the form of the objective function can then be avoided. Lately, Cheng and Chang [16,17] used the concept of the SCGM method to develop an inverse method for predicting the internal temperature distribution of PEM fuel cells. Results show that the outer surface temperature data can be used to predict the internal temperature distribution at the interface between the carbon plate and the MEA.

Under these circumstances, in the present study, a multi-parameter optimization for the geometric parameters of the PEM fuel cell based on a three-dimensional full cell model is attempted. Schematic of a single-cell PEMFC with parallel straight channels on both the anode and the cathode carbon plates is shown in Fig. 1. The single-cell PEMFC consists of a carbon plate, a gas diffusion layer (GDL), a catalyst layer, for each of the anode and the cathode sides, as well as a PEM membrane at the center. Among these possible influential geometric parameters, the gas channel width fraction (Λ), the gas channel height (h) and the thickness of the gas diffusion layer (t_{GDL}) are recognized as the influential factors affecting the behavior of the fuel cells. Therefore, these three parameters are selected as the design parameters to be optimized in the present study. For other physical and geometrical parameters of the cell shown in this figure, their values are kept constant throughout the study, which are given in Table 1.

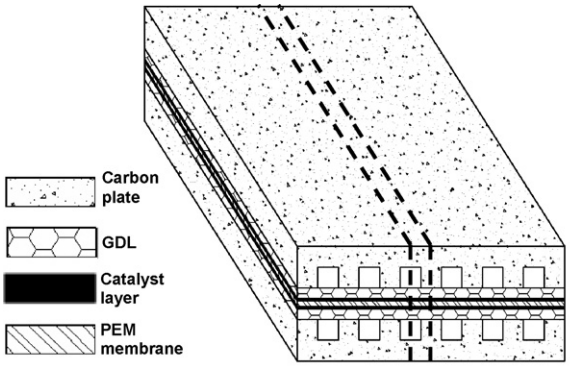

(a)

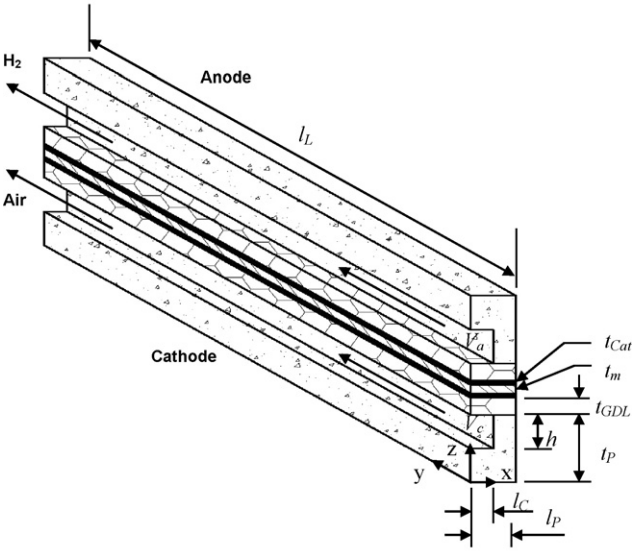

(b)

Fig. 1. Physical model of a single-cell proton exchange membrane fuel cell. (a) Single-cell model with parallel straight channels and (b) gas channel geometry.

The SCGM method [13] is employed herein as the optimization search scheme. This study is aimed at optimization of these three parameters so that the best performance of the PEMFC in prescribed operating conditions can be obtained. However, it is noted that the present optimization approach is not limited to the present group of designed parameters. When necessary, more designed parameters may be readily applied.

2. Optimization approach

The approach is developed by integrating a direct problem solver and an optimizer. The theories of the two solvers are briefly described in the following.

2.1. Direct problem solver

The following assumptions are made in prior to the construction of the governing equations of the three-dimensional full-cell model:

(1) The operating temperature is uniform and constant in the solution domain, and in this study, the operating temperature and pressure are assigned to be 323 K and 101,325 Pa, respectively.
(2) The fuel cell operates at steady state, and the operating voltage is fixed at 0.7 V.
(3) The gas flows are laminar and compressible in the gas channels and the porous layers, and effects of gravity on the flow motion are negligible.
(4) Thermodynamic and electrochemical properties of the gases and the solid materials of the fuel cell components are assumed constant.
(5) The gas diffusion layers and the catalyst layers are homogeneous, isotropic porous media.
(6) Phase change process is ignored and water exists in the entire fuel cell only in vapor phase in the simulation.

2.1.1. Electronic conduction in carbon plates, GDLs and catalyst layers

The carbon plate, the GDL and the catalyst layers all serve as conductors for electric current. In the carbon plate and the GDL, there is no electrochemical reaction taking place. The electrochemical reactions only take place in the catalyst layers. Due to the electrochemical reactions activated in the catalyst layers, there exists a source term in the electronic conduction equation. Therefore, in these three components the electronic conduction equation may be expressed in general form as

$$\nabla(\sigma^{\text{eff}}\nabla\phi) = \zeta \tag{1}$$

where ϕ is the electronic potential and σ^{eff} denotes the effective electronic conductivity. For the carbon plates, the effective

Table 1
Fixed parameters of base case

Parameter	Symbol	Value
Electronic conductivity of catalyst layer ($\Omega^{-1}\,m^{-1}$)	$\sigma_{S,Cat}$	300
Effective ionic conductivity of catalyst layer ($\Omega^{-1}\,m^{-1}$)	Γ_{Cat}^{eff}	4.2
Effective mass diffusivity of oxygen in catalyst layer ($cm^2\,s^{-1}$)	$D_{O_2,Cat}^{eff}$	1.9546×10^{-3}
Effective mass diffusivity of hydrogen in catalyst layer ($cm^2\,s^{-1}$)	$D_{H_2,Cat}^{eff}$	0.985×10^{-3}
Effective mass diffusivity of oxygen in GDL ($cm^2\,s^{-1}$)	$D_{O_2,GDL}^{eff}$	1.845×10^{-2}
Effective mass diffusivity of hydrogen in GDL ($cm^2\,s^{-1}$)	$D_{H_2,GDL}^{eff}$	0.930×10^{-2}
Effective electronic conductivity of catalyst layer ($\Omega^{-1}\,m^{-1}$)	σ_{Cat}^{eff}	135.265
Bruggemann coefficient of gas diffusion layer	χ_{GDL}	1.5
Bruggemann coefficient of catalyst layer	χ_{Cat}	1.5
GDL permeability (m^2)	k_{GDL}	1.76×10^{-11}
Catalyst layer permeability (m^2)	k_{Cat}	1.76×10^{-11}
Anode inlet gas velocity ($m\,s^{-1}$)	V_a	0.3
Cathode inlet gas velocity ($m\,s^{-1}$)	V_c	0.5
Anode inlet mass fraction of H_2	$Y_{H_2,i}$	0.445
Anode inlet mass fraction of H_2O	$Y_{H_2O,ai}$	0.555
Cathode inlet mass fraction of O_2	$Y_{O_2,i}$	0.212
Cathode inlet mass fraction of N_2	$Y_{N_2,i}$	0.709
Cathode inlet mass fraction of H_2O	$Y_{H_2O,ci}$	0.079
Operating voltage (V)	$\mathbf{V}$	0.7
Anodic charge transfer coefficients for anode reaction	$\alpha_{a,a}$	0.5
Cathodic charge transfer coefficients for anode reaction	$\alpha_{a,c}$	0.5
Anodic charge transfer coefficients for cathode reaction	$\alpha_{c,a}$	1.5
Cathodic charge transfer coefficients for cathode reaction	$\alpha_{c,c}$	1.5
Reference transfer current density at anode ($A\,m^{-3}$)	$j_{a,ref}$	9.0×10^8
Reference transfer current density at cathode ($A\,m^{-3}$)	$j_{c,ref}$	250
Anode concentration parameter	r_a	1.0
Cathode concentration parameter	r_c	1.0
Porosity of catalyst layer	$\varepsilon_{V,Cat}$	0.112
Porosity of gas diffusion layer	ε_{GDL}	0.5
Thickness of membrane (m)	t_m	1.78×10^{-4}
Electronic conductivity of gas diffusion layer ($\Omega^{-1}\,m^{-1}$)	σ_{GDL}	300
Electronic conductivity of carbon plate ($\Omega^{-1}\,m^{-1}$)	σ_P	4000
Ionic conductivity of Nafion ($\Omega^{-1}\,m^{-1}$)	$\Gamma_{N,Cat}$	25.56
Operating temperature (K)	T	323
Inlet and outlet pressure (Pa)	$\mathbf{P}_i$, $\mathbf{P}_0$	101,325
Gas channel length (m)	l_L	5.0×10^{-2}
Width of a module (m)	l_P	1.0×10^{-3}
Thickness of catalyst layer (m)	t_{Cat}	1.0×10^{-5}
Thickness of carbon plate (m)	t_P	2.0×10^{-3}
Height of gas channel (m)	h	1.0×10^{-3}

electronic conductivity σ^{eff} is treated as a constant (σ_P). For the porous gas diffusion and catalyst layers, the magnitude of the effective electronic conductivity is determined in terms of the porosity in accordance with the Bruggeman's equation as

$$\sigma_{GDL}^{eff} = (1 - \varepsilon_{GDL})^{\chi_{GDL}} \sigma_{GDL} \tag{2a}$$

$$\sigma_{Cat}^{eff} = (1 - \varepsilon_{V,Cat})^{\chi_{Cat}} \sigma_{S,Cat} \tag{2b}$$

It is noticed that the effective electronic conductivity of the catalyst layer (σ_{Cat}^{eff}) increases with the volume fraction of solid catalyst particles in catalyst layer ($\varepsilon_{S,Cat}$). In addition, the source term ζ in Eq. (1) is zero for the carbon plates or the GDL without electrochemical reaction. When the catalyst layers is dealt with, ζ is equal to the transfer current densities $-j_a$ and j_c for the anode and the cathode, respectively. The transfer current densities at the anode and the cathode are calculated based on the Butler-Volmer condition as

$$j_a = j_{a,ref}\left(\frac{Y_{H_2}}{Y_{H_2,ref}}\right)^{r_a} \times \left[\exp\left\{\frac{\alpha_{a,a}F}{RT}\eta\right\} - \exp\left\{\frac{-\alpha_{a,c}F}{RT}\eta\right\}\right] \tag{3a}$$

$$j_c = j_{c,ref}\left(\frac{Y_{O_2}}{Y_{O_2,ref}}\right)^{r_c} \times \left[\exp\left\{\frac{\alpha_{c,a}F}{RT}\eta\right\} - \exp\left\{\frac{-\alpha_{c,c}F}{RT}\eta\right\}\right] \tag{3b}$$

where $j_{a,ref}$ and $j_{c,ref}$ are the reference transfer current densities, and r_a and r_c the concentration parameters, at the anode and the cathode, respectively. In addition, $\alpha_{a,a}$ and $\alpha_{a,c}$ are the anodic and the cathodic charge transfer coefficients for anode reaction, and $\alpha_{c,a}$ and $\alpha_{c,c}$ the anodic and the cathodic charge transfer coefficients for cathode reaction. $Y_{O_2,ref}$ and $Y_{H_2,ref}$ are the reference concentrations at which the exchange current densities

were obtained. All the reference values of these coefficients are already given in Table 1. Note that the reference current densities, transfer coefficients and reference concentrations have been set so as to fit the experimental data.

2.1.2. Ionic conduction in catalyst layers and proton exchange membrane

The protons of hydrogen (H^+) are generated in the anode catalyst layer and then migrate through the proton exchange membrane toward the cathode catalyst layer to react with oxygen and the returning electrons. Therefore, ionic conduction occurs in the catalyst layers and the proton exchange membrane.

The ionic conduction equation for determination of the phase potential (φ) in the catalyst layers is

$$-\nabla(\Gamma_{\mathrm{Cat}}^{\mathrm{eff}}\nabla\varphi_{\mathrm{Cat}}) = \zeta \tag{4}$$

where φ_{Cat} is the phase potential and $\Gamma_{\mathrm{Cat}}^{\mathrm{eff}}$ is the effective ionic conductivity of the catalyst layers. Note that the source term ζ is identical to that of Eq. (1). The effective ionic conductivity $\Gamma_{\mathrm{Cat}}^{\mathrm{eff}}$ is evaluated by using

$$\Gamma_{\mathrm{Cat}}^{\mathrm{eff}} = (1-\varepsilon_{\mathrm{V,Cat}})^{\chi_{\mathrm{Cat}}}\Gamma_{\mathrm{S,Cat}} \tag{5}$$

On the other hand, the ionic conduction equation for the membrane is expressed as

$$\nabla(\Gamma_{\mathrm{m}}\nabla\varphi_{\mathrm{m}}) = 0 \tag{6}$$

where φ_{m} is the phase potential and Γ_{m} is the ionic conductivity of the membrane. The expression for ionic conductivity of the membrane has been proposed by Springer et al. [18] as:

$$\Gamma_{\mathrm{m}}(T) = \exp\left[1268\left(\frac{1}{303}-\frac{1}{T}\right)\right](0.005239\lambda - 0.00326) \tag{7}$$

where the water content of the membrane (λ) is dependent on the dimensionless water activity in the membrane (a) according to experimental data. The activity is assumed uniform over the membrane, which is defined as the gas partial pressure of water at equilibrium with the membrane divided by the saturation pressure of water vapor at the operating temperature. That is

$$a = \frac{X_{\mathrm{H_2O}}P}{P_{\mathrm{sat}}} \tag{8}$$

where the saturation pressure of water vapor can be computed from

$$\begin{aligned}\log_{10}P_{\mathrm{sat}} = {} & -2.1794 + 0.02953(T-273.15) - 9.1837 \\ & \times 10^{-5}(T-273.15)^2 + 1.4454 \\ & \times 10^{-7}(T-273.15)^3\end{aligned} \tag{9}$$

with T in K. The correlation between λ and a is derived as

$$\lambda = \begin{cases} 0.043 + 17.81a - 39.85a^2 + 36a^3 & 0 \le a \le 1 \\ 14 + 1.4(a-1) & 1 < a \le 3 \end{cases} \tag{10}$$

Based on the solutions for the phase potential (φ), the distribution of local ionic current density (i_i) may be further determined with

$$\vec{i} = -\Gamma\nabla\varphi \tag{11}$$

2.1.3. Mass, momentum and species transport in gas channels, GDLs and catalyst layers

The governing equations for the gas flows in the gas channels and the porous layers are the conservation equations of mass, momentum and species. Application of the flow channels and the gas diffusion layers in the fuel cells is to allow the reactant gases to diffuse uniformly into the catalyst layers but prevent excessive increase in electrical resistance against the released electrons from the catalyst layers. The porous layers include the gas diffusion layers and the catalyst layers, in which the mass, momentum and species equations for the flows are derived based on the non-Darcy law. These equations are given below:

Mass equation:

$$\nabla(\varepsilon\rho\vec{U}) = 0 \tag{12}$$

Momentum equation:

$$\nabla(\varepsilon\rho\vec{U}\vec{U}) = -\varepsilon\nabla P + \nabla(\varepsilon\tau) + \frac{(\varepsilon)^2\mu\vec{U}}{k} \tag{13}$$

Species equation:

$$\nabla(\varepsilon\rho U Y_i) = \nabla(D_i^{\mathrm{eff}}\nabla Y_i) + S_i \tag{14}$$

where ε and k are the porosity and the permeability of the porous layers, respectively; τ represents the fluid stress tensor. Fuel gas at the anode is considered to contain H_2 and H_2O, and oxidant gas at the cathode contains O_2, N_2 and H_2O. Y_i denotes the species mass fraction of species i. Note that for the pure fluid flows in the gas channels, the values of ε and k are given with $\varepsilon = 1$ and $k = \infty$.

Calculation for the effective mass diffusivity of species i (D_i^{eff}) is based on Bruggeman's equation, that is

$$D_i^{\mathrm{eff}} = (\varepsilon)^{\chi}D_i \tag{15}$$

where D_i is the mass diffusivity of species i and χ is the Bruggemann coefficient of the porous layer.

2.1.4. Electrochemical reaction in catalyst layers

In Eq. (14), the term S_i stands for the source term of species i coming from the electrochemical reactions in the catalyst layers. Note that H_2 and O_2 are consumed by the reactions in the catalyst layers of anode and cathode, respectively, and H_2O is the product of the reaction at the cathode. Therefore, the source terms for different species are

$$S_{\mathrm{H_2}} = -\frac{j_{\mathrm{a}}}{2F} \tag{16a}$$

$$S_{\mathrm{O_2}} = \frac{j_{\mathrm{c}}}{4F} \tag{16b}$$

$$S_{\mathrm{H_2O}} = -\frac{j_{\mathrm{c}}}{2F} \tag{16c}$$

where j_{a} and j_{c} are calculated with Eqs. (3a) and (3b).

Owing to the flexibility that a commercial computational fluid dynamics code may have in dealing with the complex three-dimensional problems, these above set of conservation equations along with the property equations are solved by adopting a finite-volume scheme on structured grids within the framework of the commercial code CFD-ACE + released by ESI-CFD Inc.

2.1.5. Boundary conditions

For the pattern of straight parallel channels shown in Fig. 1, a periodic transport phenomenon is expected to develop from channel to channel as long as the number of gas channels is large enough. Thus, one only needs to deal with the solution domain of a single module, with the periodic boundary conditions on the faces indicated by the dashed lines. In this study, the width of a module (l_P) is set to be 1 mm. Therefore, for the faces of solution domain at $x = 0$ and 1 mm, a periodic boundary condition for $\vec{U}$, Y, ϕ and φ is prescribed.

As to the inlet conditions, the inlet velocities for the anode gas (hydrogen) and the cathode gas (air) in the gas channel, V_a and V_c, are fixed at 0.3 and 0.5 m s^{-1}, respectively. The inlet mass fractions for all the gas species are specified, and their values are provided in Table 1. On the other hand, for the boundary conditions at the exit, it is assumed that the flow becomes fully developed downstream. Thus, the exit boundary conditions may be described as

$$u = w = \frac{\partial v}{\partial y} = \frac{\partial Y_i}{\partial y} = \frac{\partial \phi}{\partial y} = \frac{\partial \varphi}{\partial y} = 0 \tag{17}$$

Solid walls of the gas channels or the carbon plates are impermeable, and hence, on the solid walls, $\partial Y_i/\partial n = 0$ and $\vec{U} = 0$. In addition, since both the gas channels and the membrane are insulators against electrons; at the boundaries of the gas channels and the membrane, the normal gradient of the electric potential is zero, that is, $\partial\phi/\partial n = 0$. Furthermore, the ionic conduction takes place only inside the catalyst layer and proton exchange membrane, and the protons are not allowed to transfer into other components; therefore, on the faces of the catalyst layer and the membrane the normal gradient of phase potential is assigned to be zero.

The average current density (**I**) of fuel cells is calculated by integration of local electric current density distribution on the carbon plate surface at $z = 0$ divided by the carbon plate surface area as

$$\mathbf{I} = \frac{1}{A}\int_0^A i_s \, dA \tag{18}$$

where i_s is the local electric current density on the carbon plate surface and A is the carbon plate surface area. In the mean time, the gas channel width fraction (Λ) is defined by the ratio of the gas channel width (l_C) to the width of a module (l_P), that is

$$\Lambda = \frac{l_C}{l_P} \tag{19}$$

It is important to note that the direct solver used in the present work is a single-phase fuel cell model with electron transport explicitly taken into account. The inclusion of electron transport in the fuel cell modeling is required particularly when the effect of the gas channel width fraction is considered. For further information about the modeling for the electron transport, one may refer to the work of Meng and Wang [19].

2.2. Optimizer

In this study, the SCGM method [10] is employed to construct the optimizer for seeking the optimal values of the design parameters. The objective function in conjunction with the optimization process is defined in the following:

$$J(e_k) = 1/\mathbf{P}, \quad k = 1\text{–}3 \tag{20}$$

where e_k ($k = 1$–3) represent the design parameters, i.e. gas channel width fraction (Λ), the gas channel height (h) and the thickness of the gas diffusion layer (t_{GDL}). The power density of the fuel cell is the product of the cell voltage (**V**) and the electric current density (**I**) as $\mathbf{P} = \mathbf{I} \times \mathbf{V}$. In this manner, the power density (**P**) is expected to reach a maximum as the magnitude of the objective function (J) is minimized. In the SCGM method, the values of the step size (β_k) during the searching procedure are fixed. The initial guess for each design parameter is made first, and in the successive steps the conjugate-gradient coefficients and the searching directions are evaluated. The new design variables are continuously updated. When the objective function reaches a minimum, the optimization process is completed and the searching procedure is then terminated.

The procedure in the optimizer is presented as follows:

(1) Make the initial guess for the designed parameters e_k, assign the values to the step sizes β_k.
(2) Specify all boundary conditions, and then solve the physical problem by the numerical simulator.
(3) Calculate the objective function $J(e_k, k = 1\text{–}3)$. If the convergence criterion is satisfied as the objective function reaches a minimum in the iterating process, the solution process is terminated. Otherwise, proceed to step (4).
(4) Calculate the gradient functions of the function J by the sensitivity analysis of numerical direct differentiation [13]:

$$\frac{\partial J^n}{\partial e_k} = \frac{\Delta J^n}{\Delta e_k}, \quad k = 1\text{–}3 \tag{21}$$

(5) Calculate the conjugate-gradient coefficients $\gamma_k^n (k = 1\text{–}3)$:

$$\gamma_k^n = \left[\frac{(\partial J/\partial e_k)^n}{(\partial J/\partial e_k)^{n-1}}\right]^2, \quad k = 1\text{–}3 \tag{22}$$

For the first step with $n = 0$, $\gamma_k^0 = 0$.
(6) Calculate the searching directions $\xi_k^n (k = 1\text{–}3)$:

$$\xi_k^{n+1} = \frac{\partial J^n}{\partial e_k} + \gamma_k^n \xi_k^n, \quad k = 1\text{–}3 \tag{23}$$

(7) Update new design variables by

$$e_k^{n+1} = e_k^n - \beta_k \xi_k^{n+1}, \quad k = 1\text{–}3 \tag{24}$$

and then return to step (2).

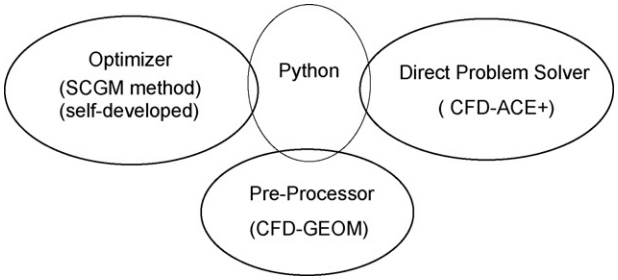

Fig. 2. Connection between optimizer and direct problem solver.

2.3. Connection between direct problem solver and optimizer

The self-developed optimizer and the computational fluid dynamics code with the pre-processor are connected through an interface program. The interface programs are developed by using the Python language. Connection among the optimizer and the direct problem solver is shown in Fig. 2. Through the Python-interface connection, the message of any change in the design parameters suggested by the optimizer is firstly sent to the pre-processor for updating the grid system and the boundary conditions. Secondly, the CFD code is executed based on the updated grid system and boundary conditions to yield the numerical solutions for distribution of $\vec{U}$, Y, ϕ and φ in all the components of the fuel cell. The solutions obtained from the direct problem solver are then used to calculate the value of the objective function, which is further transmitted back to the optimizer for calculating the consecutive searching directions. Flow chart of the optimization process is plotted in Fig. 3.

2.4. Experiments for validation

To verify the numerical predictions of the direct problem solver, a single-cell fuel cell module with cross-sectional area of 22 cm × 22 cm and active area of 14 cm × 14 cm has been installed and tested. Two 3-mm thick composite graphite plates are used as the flow fields and current conductors. A five-layer membrane exchange assembly (MEA) is placed at the center between the two composite graphite plates. The membrane used in this MEA is Nafion® 112 and the gas diffusion layers are made of carbon fiber paper. Meanwhile, in the experiments the volumetric flow rates of the hydrogen and the air are typically maintained at 1500 and 2500 sccm, corresponding to $V_a = 0.3\ m\ s^{-1}$ and $V_c = 0.5\ m\ s^{-1}$, respectively. The hydrogen and the air are humidified to reach 100% relative humidity and 80 °C temperature before entering the gas flow channels. The operating and geometrical conditions given to the direct problem solver are consistent with the experiments. The fuel cell temperature is maintained at 343 K.

Fig. 4 shows a comparison between the numerical predictions and the experiment data for the polarization curves of the single-cell fuel cell module. It is observed that the numerical predictions closely agree with the experiments, especially in the regime of $\mathbf{I} < 3800\ A\ m^{-2}$. Over this regime, the experimental data appear to experience a greater drop in the operating voltage than the pre-

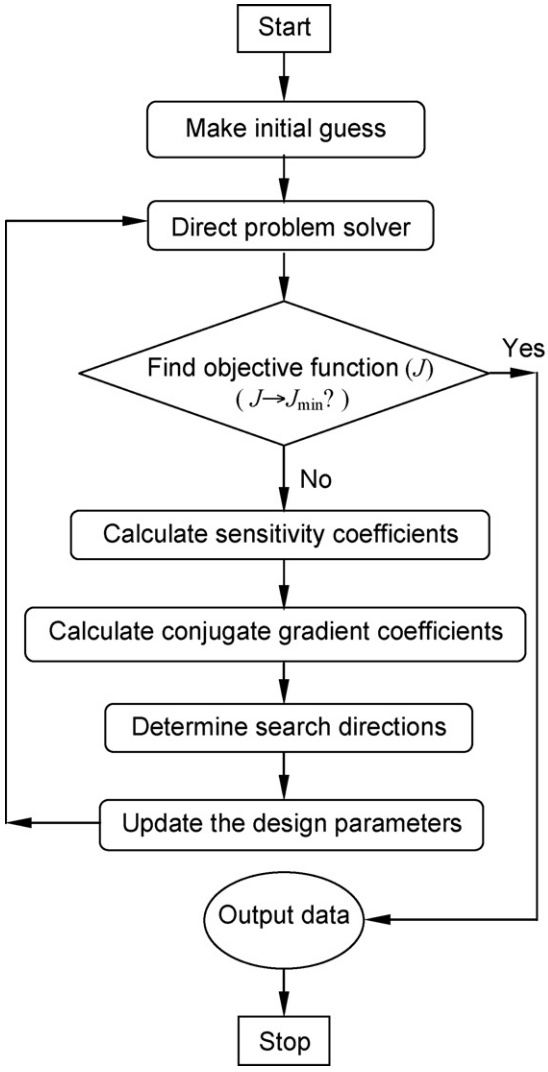

Fig. 3. Flow chart of the optimization process.

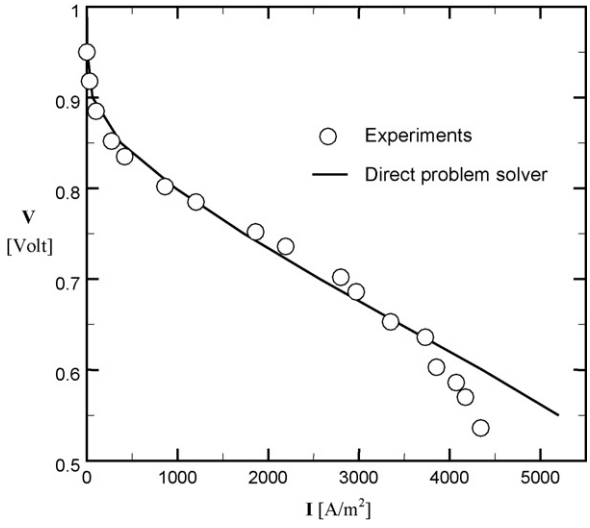

Fig. 4. Comparison in polarization curves between predictions and experiments.

dicted. The greater voltage drop is attributed to the concentration loss due to insufficient supply of O_2 and H_2 in experiments at the cathode and the anode, respectively. Nevertheless, in this figure it is found that at $\mathbf{V} = 0.7$ V the numerical and the experimental data for the current density are in close agreement (at approximately 2500 A m^{-2}). Thus, the typical value of the operating voltage of the fuel cell is fixed at 0.7 V in the present study to determine the optimal parameters.

3. Results and discussion

3.1. Parametric study

In addition to the experimental demonstration shown earlier, the direct problem solver's capability of providing numerical predictions under various conditions is further studied herein.

Numerical predictions of the mass fraction distributions of oxygen and hydrogen at the cathode and the anode sides, respectively, on cross section at $y = 25$ mm with different channel width fractions ($\Lambda = 0.6$, 0.4 and 0.2) are shown in Fig. 5. In the mean time, planar distributions of oxygen mass fraction distribution at the center plane of the cathode catalyst layer with different channel width fractions are displayed in Fig. 6. The interface between the gas channel and the rib is indicated by the dashed lines. It is expected that a larger channel width fraction leads to sufficient gases supply into the catalyst layer for electrochemical reaction. The results shown in the two figures clearly match this expectation. As observed in Figs. 5 and 6, the concentrations of the reactants are higher in the gas channels at $\Lambda = 0.6$, whereas at $\Lambda = 0.2$ the concentrations of the reactants are significantly increased. However, note that a larger channel width also gives narrower ribs which serve as electron-conduction pas-

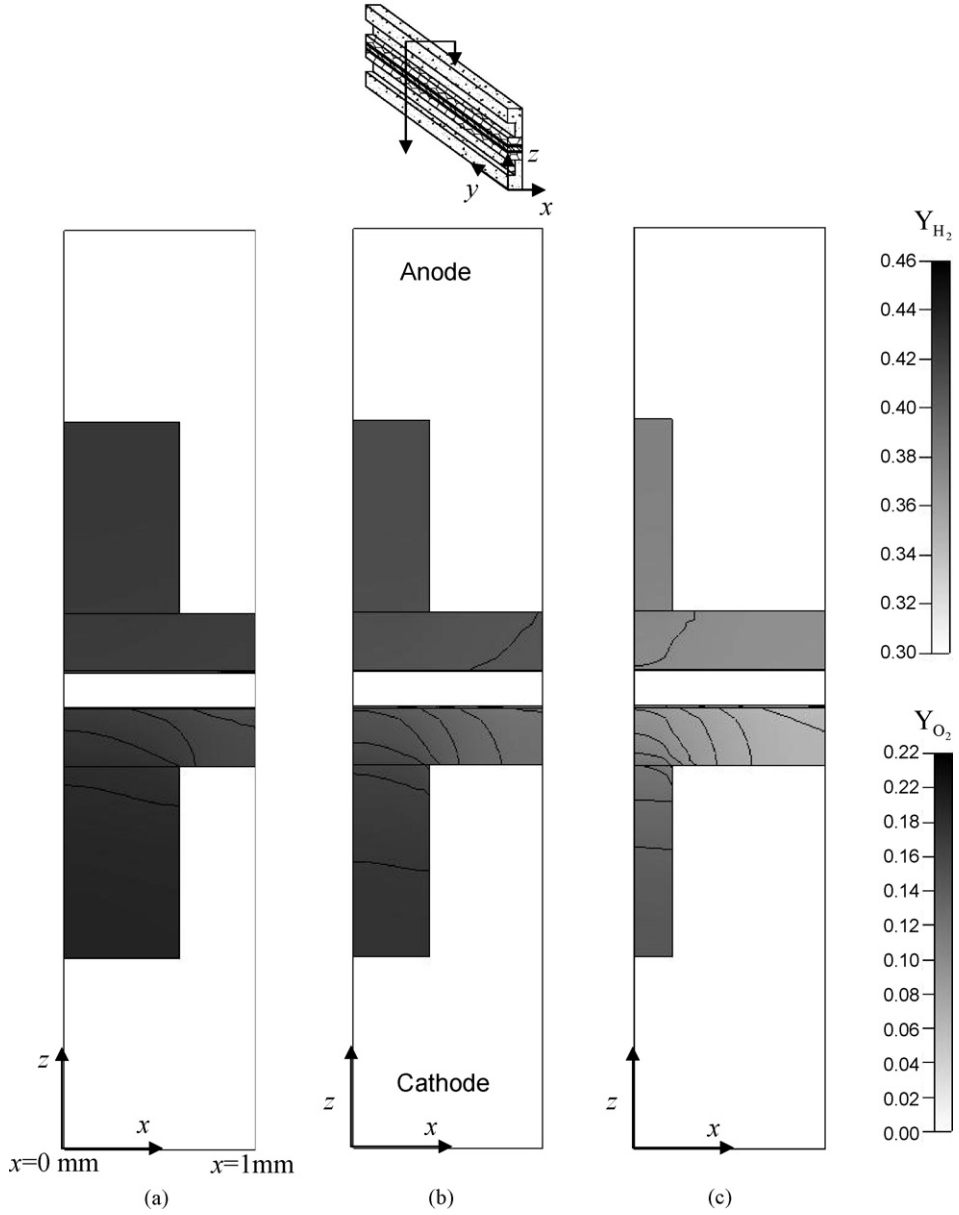

Fig. 5. Mass fraction distributions on cross section at $y = 25$ mm with different channel width fractions (dashed line indicates that interface between channel and rib): (a) $\Lambda = 0.6$, (b) $\Lambda = 0.4$ and (c) $\Lambda = 0.2$.

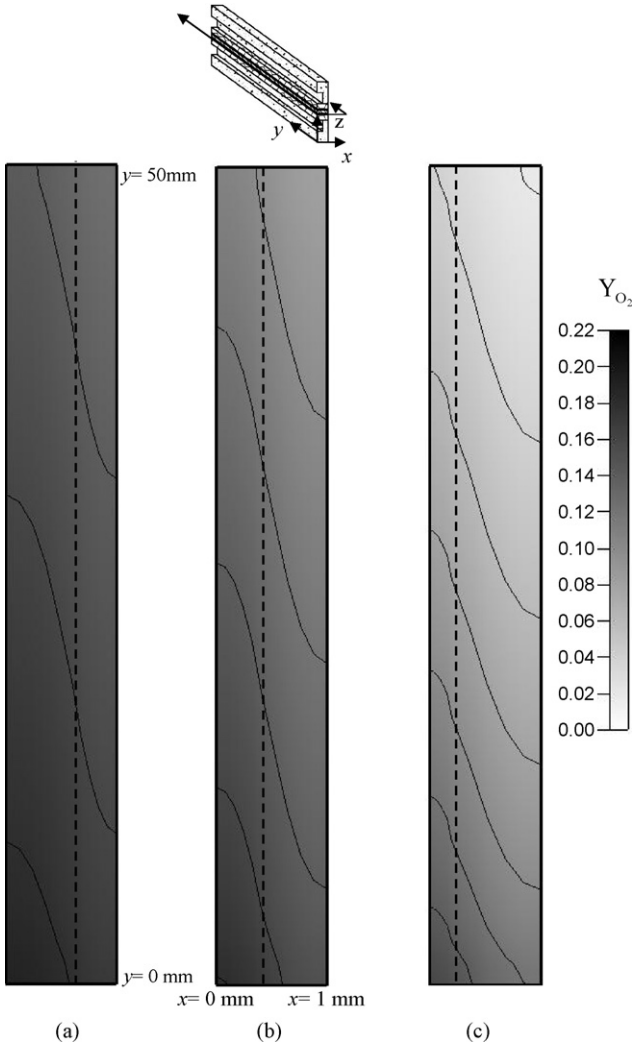

Fig. 6. Planar distributions of oxygen mass fraction distribution at the center plane of the cathode catalyst layer with different channel width fractions (dashed line indicates that interface between channel and rib): (a) $\Lambda = 0.6$, (b) $\Lambda = 0.4$ and (c) $\Lambda = 0.2$.

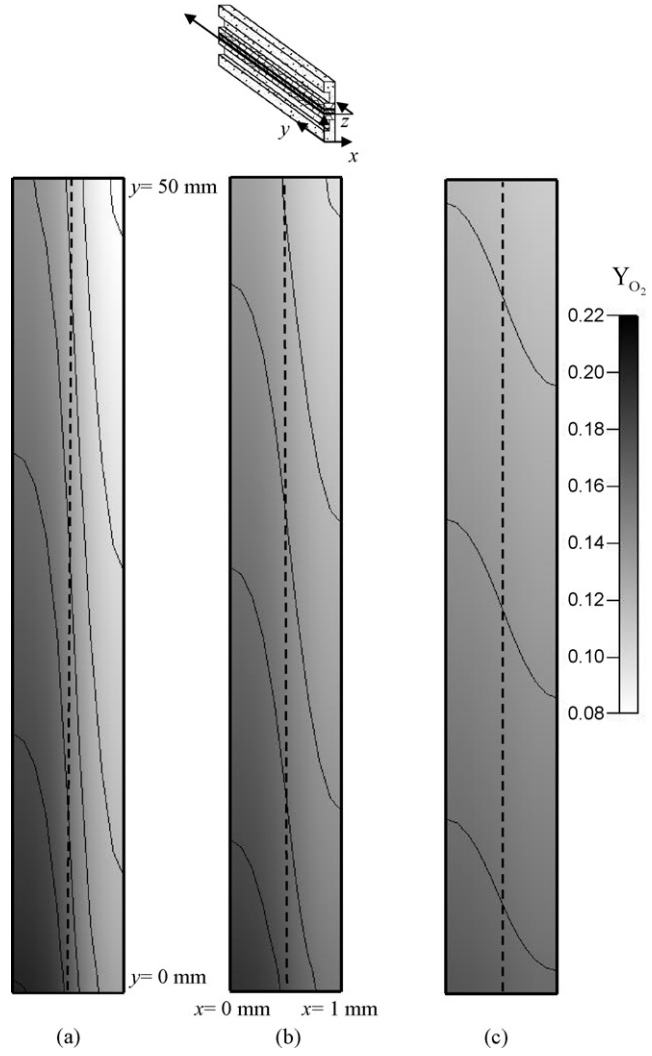

Fig. 7. Planar distributions of oxygen mass fraction distribution on the center plane of the cathode catalyst layer with different thicknesses of gas diffusion layer (dashed line indicates that interface between channel and rib): (a) $t_{GDL} = 1 \times 10^{-4}$ m, (b) $t_{GDL} = 2 \times 10^{-4}$ m and (c) $t_{GDL} = 5 \times 10^{-4}$ m.

sages; therefore, an increase in the gas channel fraction is always accompanied by an increase in the ohmic impedance. With these two opposing effects, there should exist a desired optimal value of the gas channel width fraction.

Fig. 7 conveys the distributions of oxygen mass fraction distribution on the center plane of the cathode catalyst layer with different thicknesses of gas diffusion layer (t_{GDL}). The thickness of the gas diffusion layer is assigned to be 1×10^{-4}, 2×10^{-4} and 5×10^{-4} m. It is observed in Fig. 7(c) that a thicker gas diffusion layer (say, 5×10^{-4} m) may allow the reactant gas to diffuse more uniformly in the entire gas diffusion layer before penetrating into the catalyst layer. Hence, on the center plane of the cathode catalyst layer, a very uniform concentration distribution can be seen. On the other hand, in Fig. 7(a) for the case at $t_{GDL} = 1 \times 10^{-4}$ m, the oxygen concentration is appreciably higher in the area adjacent to the gas channel than in the area adjacent to the rib. However, an increase in the thicknesses of gas diffusion layer also tends to increase the electric resistance against the conduction of electrons. Here, one finds another influential parameter that is worth further study.

Plotted in Fig. 8 are the local current density distributions on the center plane of the cathode catalyst layer with different channel heights (h). In this figure, the gas channel height is assigned to be 4×10^{-4}, 8×10^{-4} or 16×10^{-4} m. Mass flow rates of the reactant gases can be elevated by increasing the height of gas channels, so as to provide more gases for reaction; however, higher channels may also slightly elevate the ohmic impedance of the fuel cell. It is indeed observed in Fig. 8 that the magnitude of the local current density is higher in the area adjacent to the rib since the rib serves as passage for electron conduction. Meanwhile, local current density becomes stronger on the entire plane when the channel height becomes lower.

3.2. Optimization of PEM fuel cell

In the parametric studies considered above, only one parameter is changed while others are fixed. In fact, multi-parameter

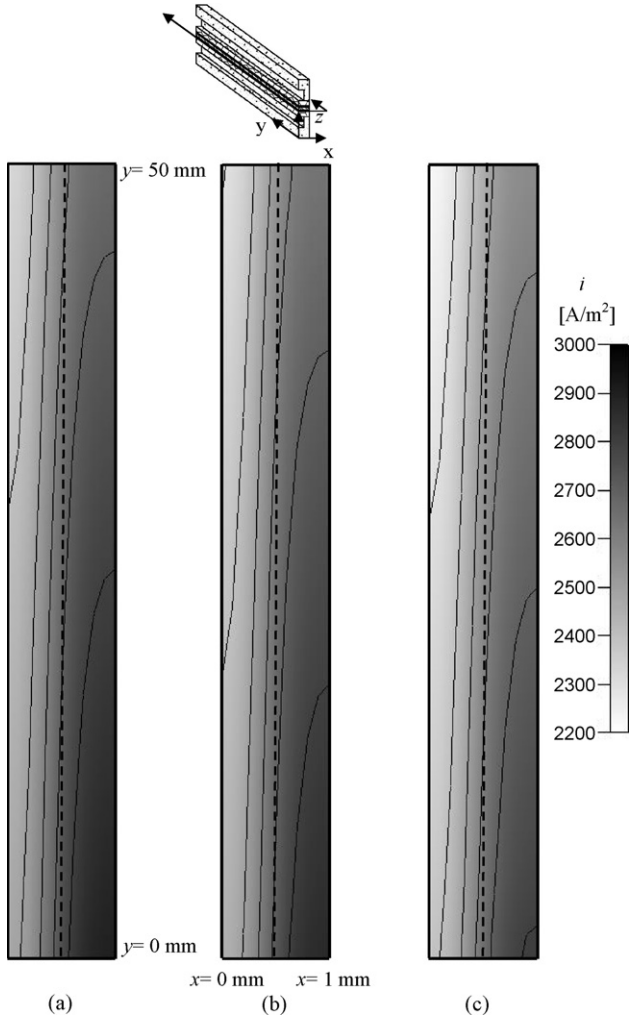

Fig. 8. Local current density distributions on the center plane of the cathode catalyst layer with different channel heights (dashed line indicates that interface between channel and rib): (a) $h = 4 \times 10^{-4}$ m, (b) $h = 8 \times 10^{-4}$ m and (c) $h = 16 \times 10^{-4}$ m.

optimization is more meaningful in practices. Design of the geometric parameters is now carried out to optimize the performance of PEMFC by integrating the direct problem solver with the optimizer.

Attention is now drawn to the results of optimization for the geometric parameters, Λ, t_{GDL} and h. Trajectory of the optimization process seeking an optimal set of these design parameters is shown in Fig. 9. The optimal combination is sought in the parameter space (Λ, t_{GDL}, h). The optimization process is started with the original design of $\Lambda = 0.8$, $t_{GDL} = 1$ mm and $h = 0.8$ mm. It can be observed in Fig. 9 that the SCGM optimizer effectively brings the searching process to approach the optimal state. In this case, it is found that the iteration is converged after about 30 iterations. The computation time required is approximately 60 h on a personal computer with an AMD-3GMHz CPU. Based on the results shown in Fig. 9, it is found that at $\Lambda = 0.3925$, $t_{GDL} = 0.176$ mm and $h = 1.2034$ mm, the optimization process reaches a maximum power of 1857 W m^{-2}. The variation of power density during the optimization process is shown in Fig. 10. Note that the power density associated with

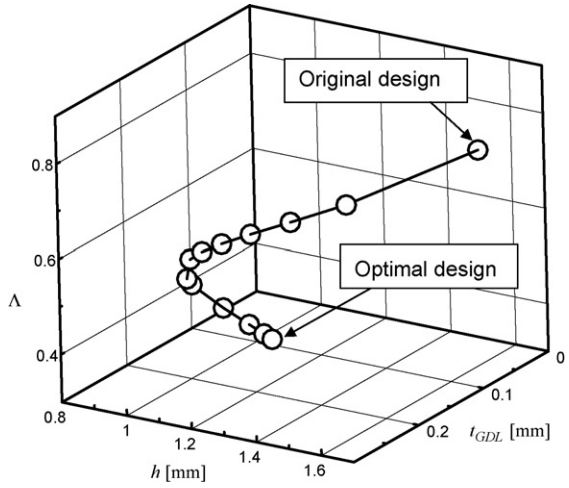

Fig. 9. Trajectory of the optimization process for a PEM fuel cell seeking an optimal set of designed parameters, Λ, t_{GDL} and h.

the original design is approximately 1400 W m^{-2}. The power density then approaches its maximum value when the optimal parameters are obtained. As a result, the optimization process leads to an increase by 457 W m^{-2} (32%) in the power density.

Fig. 11 shows the comparison in performance curve between the original and the optimal design obtained by the optimizer. Results show that the present approach can yield an optimal design having higher performance than the original one. Based on the features of the curves, it is recognized that the optimal design is greatly improved not only in the ohmic loss but also in the limiting current density.

In order to ensure the robustness of the optimizer, Fig. 12 shows the convergence of the optimization process from three different initial combinations of the three parameters, Λ, t_{GDL} and h. It can be observed in this figure that the present approach leads to the same optimal set of parameters from different initial guesses.

Note that the suggested optimal parameters are obtained under the base case conditions considered in the present study. When the conditions are changed, the optimal values of these

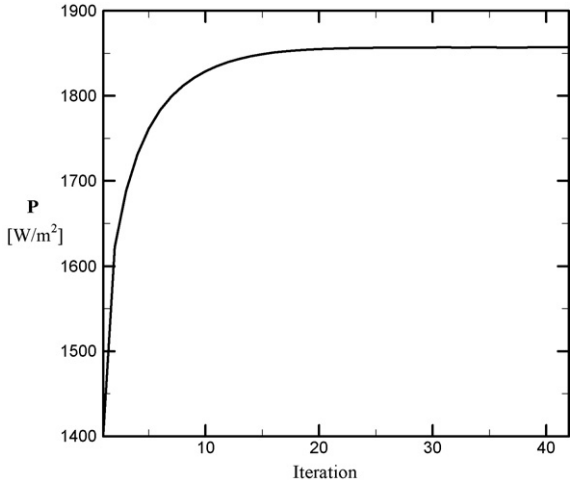

Fig. 10. Variation in power density during the optimization process.

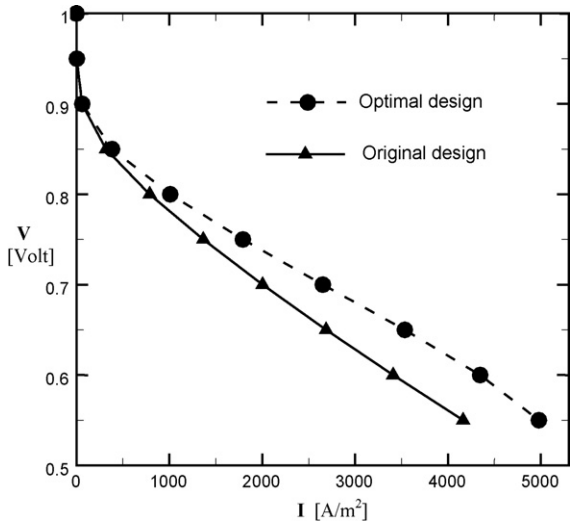

Fig. 11. Comparison in the polarization curves between the original and the optimal designs.

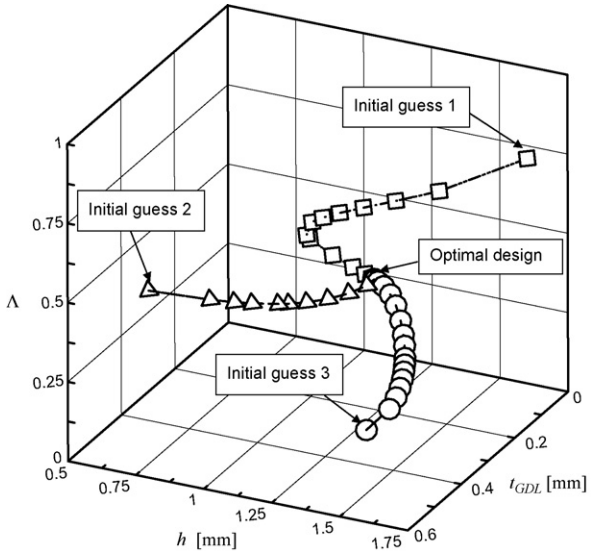

Fig. 12. Trajectories of the optimization processes from different sets of initial guesses for Λ, t_{GDL} and h.

parameters may be altered. It is also important to note that extension of the present method to the design with more parameters is a worthwhile work in the future, and a more comprehensive model would also be desired.

4. Conclusions

The present study is concerned with the development of an numerical approach which is applied for optimization of the geometric parameters of the PEM fuel cells. The approach is successfully developed by integrating a direct problem solver with an optimizer. A commercial computational fluid dynamics code is used as the direct problem solver, which is used to simulate the three-dimensional mass, momentum and species transport phenomena as well as the electron- and proton-transfer process taking place in a PEMFC. On the other hand, the SCGM method [10] is employed to build the optimizer, which is combined with the direct problem solver in order to seek the optimal geometric parameters. In this study, geometric parameters including the gas channel width fraction, the gas channel height and the thickness of the gas diffusion layer are regarded as the major factors to optimize.

A 22 cm × 22 cm single-cell fuel cell module with 14 cm × 14 cm active area has been installed and tested. The numerical predictions by the direct problem solver have been verified by the experiments.

For the particular conditions considered in this study, it is found that that at $\Lambda = 0.3925$, $t_{GDL} = 0.176$ mm and $h = 1.2034$ mm, the optimization process reaches a maximum power density of 1857 W m^{-2}, with an increase of 457 W m^{-2} (32%) compared with the original design.

It is also found that the present approach can be applied to determine the optimal set of geometric parameters, and the search process is robust and always leads to a unique final solution regardless of the initial guess.

Note that the suggested optimal parameters are obtained under the base case conditions considered in the present study. When the conditions are changed, the optimal values of these parameters may be altered.

Acknowledgements

The authors would like to thank the National Science Council, Taiwan, ROC, for their financial support under Grant: NSC 93-2212-E-036-001. Authors would also like to thank Tatung Company for their support of the experimental system.

References

[1] J.T. Wang, R.F. Savinell, Electrochim. Acta 37 (1992) 2737–2745.
[2] J.S. Yi, T.V. Nguyen, J. Electrochem. Soc. 146 (1999) 38–45.
[3] V. Gurau, F. Barbir, H. Liu, J. Electrochem. Soc. 147 (2000) 4485–4493.
[4] S. Um, C.Y. Wang, K.S. Chen, J. Electrochem. Soc. 147 (2000) 4485–4493.
[5] W. Sun, B.A. Peppley, K. Karana, J. Power Sources 144 (2005) 42–53.
[6] E. Hontanon, M.J. Escudero, C. Bautista, P.L. Garcia-Ybarra, L. Daza, J. Power Sources 86 (2000) 363–368.
[7] T. Berning, N. Djilali, J. Power Sources 124 (2003) 440–452.
[8] C.Y. Wang, Chem. Rev. 104 (2004) 4727–4766.
[9] I. Mohamed, N. Jenkins, J. Power Sources 131 (2004) 142–146.
[10] M. Grujicic, K.M. Chittajallu, Chem. Eng. Sci. 59 (2004) 5883–5895.
[11] M. Secanell, et al., Electrochim. Acta 52 (2007) 2668–2682.
[12] H.H. Lin, C.H. Cheng, C.Y. Soong, F. Chen, W.M. Yan, J. Power Sources 162 (2006) 246–254.
[13] C.H. Cheng, M.H. Chang, Numer. Heat Transfer B 43 (2003) 489–507.
[14] Y. Hung, N.G. Zamani, Appl. Math. Comput. 80 (1996) 155–179.
[15] P.C. Tuan, M.C. Ju, Numer. Heat Transfer B 37 (2000) 247–265.
[16] C.H. Cheng, M.H. Chang, J. Power Sources 139 (2005) 115–125.
[17] M.H. Chang, C.H. Cheng, J. Power Sources 142 (2005) 200–210.
[18] T.E. Springer, T.A. Zawodzinski, S. Gottesfeld, J. Electrochem. Soc. 138 (1991) 2334–2342.
[19] H. Meng, C.Y. Wang, J. Electrochem. Soc. 151 (2004) A358–A367.